ACS OMEGA

Article

Cite This: ACS Omega 2019, 4, 14369−14377

http://pubs.acs.org/journal/acsodf

Structural and Electronic Properties of Iron-Doped Sodium Montmorillonite Clays: A First-Principles DFT Study

Camila R. Ferreira,[†] Sandra H. Pulcinelli,[†] Luisa Scolfaro,[‡] and Pablo D. Borges*[,§]

[†]Instituto de Química, Universidade Estadual Paulista (IQ/UNESP), 14800-060, Araraquara, Brazil

[‡]Department of Physics, Texas State University, San Marcos, Texas 78666, United States

[§]Instituto de Ciências Exatas e Tecnológicas, Universidade Federal de Viçosa, 38810-000 Rio Paranaíba, Brazil

Supporting Information

ABSTRACT: First-principles calculations done via density functional theory were used to study the structural and electronic properties of sodium montmorillonite clay (Mt-Na^+) of general formula $M_xAl_3Si_8O_{24}H_4Na{\cdot}nH_2O$ (M_x: Mg or Fe). The final position of the interlamellar sodium atom is found to be close to the oxygen atoms located on the upper surface of silica. Following Fe-Mt-Na^+ system relaxation, with subsequent analysis of magnetic moment and magnetic states, the electroneutrality of the system established that both Fe^{2+} and Fe^{3+} oxidation states are possible to occur. The Mg^{2+}-Mt-Na^+ material shows a band gap energy greater than that of Fe^{2+}-Mt-Na^+ when iron is in the octahedral site. It is found that the valence-band maximum and the conduction-band minimum of iron-doped montmorillonite are both at the Γ-point, while it is at $V \rightarrow \Gamma$ for magnesium-doped montmorillonite. The calculated band gap from hybrid functional (HSE06) of Fe^{2+}-Mt-Na^+ is equal to 4.3 eV, exhibiting good agreement with experimental results obtained from ultraviolet−visible spectroscopy of the natural Mt-Na^+ (Cloisite-Na^+).

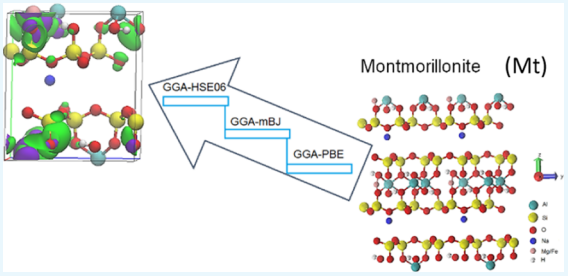

1. INTRODUCTION

Clays, the most abundant minerals found on the surface of the earth, are a natural material of texture and fine granulation and can be classified as cationic (montmorillonites = Mt or other smectites) and anionic (lamellar double hydroxides LDH). The cationic variety consist of materials with negatively charged aluminosilicates layers and interlamellar cations neutralizing the charges. The anionic variety are clay materials containing anions in the interlamellar domain.[1,2] The montmorillonites belong to the 2:1 group of filosilicates, whose structure consists of two tetrahedral (T) sheets of silica with an octahedral (O) center sheet of alumina joined together by oxygen atoms that are common to both sheets (T−O−T).[3] The stacking of these layers is governed by relatively weak short-range attractive van der Waals forces. Different isomorphic substitutions can occur, where the most common substitutions responsible for negatively charged layers are Al^{3+} by Mg^{2+}, Fe^{2+}, or Fe^{3+} in octahedral coordination and Si^{4+} by Al^{3+} or Fe^{3+} in tetrahedral coordination. To compensate the negative charges, the interlamellar region is occupied by cations such as Na^+, K^+, and Ca^{2+}.[1−4] Different kinds of isomorphic substitutions in the lamellae as well as in the cations in the interlamellar region bring distinct physical and chemical properties to montmorillonite. Moreover, these layered structures are also possible to occur through charge balance, leading the systems to an equilibrium state. Sainz-Dias et al. reported different results for montmorillonites with isomorphic substitution of Si^{4+} by Al^{3+} and Fe^{3+} in the tetrahedral coordination layer, where the trivalent cations are responsible for the layer charge. The authors obtained similar behavior for Al^{3+} replaced by Fe^{3+} in the octahedral layer where other atoms, such as Mg^{2+} octahedrally coordinated, are responsible for the excess of negative charge in the system, or yet Al^{3+} and Fe^{3+} in the tetrahedral layer.[5,6] A few other studies have shown mixing of Al, Fe, and Mg in the octahedral layer, where in this case magnesium is responsible for the negative charge in the structure.[7,8]

Polymer−clay nanocomposites present improved flame retardancy and thermal properties as compared to those of the pristine polymer matrix. The physical barrier induced by the clay and radical trapping assisted by the presence of selected 3d atoms in the inorganic phase are responsible for these properties. Carvalho et al.[9,10] have shown that structural Fe^{3+} atoms in the octahedral layer of natural Mt are reduced into Fe^{2+} due to trapping of radicals formed during poly(methyl methacrylate) (PMMA) thermal decomposition by in situ structural monitoring of PMMA-Mt thermal degradation. The presence of iron in the clay composition improves the polymer thermal stability, while the nanoconfinement created by clay layers induces radical recombination with iron and consequently delays depolymerization.[9,10]

It has also been demonstrated that iron-modified montmorillonite interacts strongly with organic materials.[11] Moreover, the combination of mineral clay with iron, aiming to produce

Received: March 12, 2019
Accepted: August 13, 2019
Published: August 27, 2019

DOI: 10.1021/acsomega.9b00685
ACS Omega 2019, 4, 14369−14377

magnetic adsorbents, has shown to be a promising material to remove organic pollutants in wastewater. This is possible because magnetic adsorbents have active sites with affinity for organic and/or inorganic compounds that, after adsorption, can be separated from the medium by an external magnetic field.[12,13]

The characterization of the smectites is usually done by observing the diffraction plane d_{001} that corresponds to the basal spacing between the lamellae. The basal spacing (lattice parameter c) corresponding to the peak d_{001} of a smectite can vary greatly, depending on the isomorphic substitution and the nature of cations exchange. The ability to exchange interplanar cations of Mt clays, known as cation exchange capacity, varies in the range of 80−150 mequiv/100 g, and the main technological properties of smectites are complemented by their high surface areas, in the range of 75−150 m^2/g^2,[14] making them efficient adsorbents, in particular, to the removal of metallic ions from the environment.[15] Likewise, these materials have wide industrial applications, such as catalysts,[16] support and catalyst precursors such as adsorbents and ion exchangers, and lamellar nanofillers in polymer nanocomposite materials,[17,18] among others. Mt-Na^+ is also a good filter for pollutants such as nitrobenzene[19] and methylene blue[11] and is a practical and promising solid electrolyte material due to the conductance properties of high valence ions therein.[20] In all of these applications, a good understanding of the montmorillonite structure is crucial.

Computational simulations provide a powerful tool to determine the most probable positions of the cations in the lamellae, as well as the number of cations in the interlamellar domain. Tavares et al. and Costa et al., using ab initio density functional theory (DFT) calculations with periodic boundary conditions, were able to accurately predict crystallographic and electronic properties of clays such as double lamellar hydroxides.[21,22] There are several theoretical studies that analyze the hydration of ions confined in the interlayer space of montmorillonites,[23−26] investigations that involve the interaction of organic components which exploit the adsorptive properties of Mt[27−31] for application as adsorbent of pollutants, and other medical applications.

Only few ab initio density functional theory (DFT) studies have considered the smectites dehydrated phases.[25,26] Fonseca et al. investigated the structure of the dehydrated montmorillonite with isomorphic substitutions of Al^{3+} by Mg^{2+} in the tetrahedral layer, and Si^{4+} by Al^{3+} in the octahedral layer. Particularly, this study shows the relation to the atomic arrangements within the lamellae comparing DFT calculations and the results of nuclear magnetic resonance (NMR) experiments. DFT based studies have shown to be a valuable method for describing the structures and dehydration of the Mt-Na^+ compound.[32] Such studies reinforce that the dehydrated montmorillonite is potential for the synthesis of, for example, nanocomposites based on hydrophobic polymers such as PMMA, which exhibits low polymerization in the presence of water.[33]

Taking into account the present studies that modify smectite clays with iron, the montmorillonite chemical formula was assumed to be $M_xAl_3Si_8O_{24}H_4Na$ (M_x: Mg and Fe), similar to that of pyrophyllite ($Si_8Al_4O_{20}(OH)_4$), also a member of the smectite clay group. The structure of Mt is similar to that of pyrophyllite,[14] nearsighted for the appropriate isomorphic substitution. The calculations presented in this work were performed on the dehydrated montmorillonite.

Based on theoretical works on clays,[21−29] they have been shown to be suitable to construct the montmorillonite system by using the supercell approach that allows for the successfully description of the tetrahedral and octahedral lamellae, as well as the interlamellar region. The modeling of these compounds can be done using, as basis, the structure of the phyllosilicate 2:1, through the isomorphic substitution of (i) Al atoms by Mg or Fe atoms in the octahedral sheet, (ii) Si atoms by Fe, and the intercalation of cations such as Na^+ in the interlamellar region. This model is widely adopted in several studies[32,35,36] since it provides the possibility of determining (i) the most probable positions of cations in lamellae, (ii) the difference in charge densities between lamella, (iii) different intercalated cations and its dependence on interlayer cation species, and (iv) the type of isomorphic substitution. Additionally, in contrast to these extensive simulation studies that have been carried out in the last decade, recent very few theoretical works focus on structural and electronic properties of the montmorillonite doped with magnesium and no studies have been found in which iron is present in the structure. In particular, an ab initio investigation of montmorillonite is still lacking.

In this work, a series of first-principles DFT calculations of the montmorillonite is reported by employing different approaches for the exchange−correlation potential for each studied system. The structural and electronic properties of Mt-Na^+ isomorphically replaced by Mg and Fe are obtained, and results for band structures, density of states, and magnetic properties are discussed. Moreover, in this work is shown the results of ultraviolet−visible (UV−vis) spectroscopy experiments performed with pristine sodium Mt clays (Cloisite-Na^+). The experimental results confirm the theoretical predictions.

2. COMPUTATIONAL METHODOLOGY

Ab Initio Study. All of the calculations were performed within the DFT.[41−44] The projector augmented wave method as implemented in the Vienna ab initio simulation package[45,50−52] was employed in this study. For the exchange−correlation potential, the generalized gradient approximation within the Perdew, Burke, and Ernzerhof (GGA-PBE) approach was adopted. We also used the modified Becke−Johnson (GGA-mBJ) potential approximation[46,47] to investigate the improvement in the band gap value. Additionally, also used here is the modified hybrid functional in mBJ which has the exchange term proposed by Beck[48] and the correlation term as proposed by Heyd−Scuseria−Ernzerhof[49] (HSE06), which is found to greatly improve the band gap description.[50−52]

The supercell model[34] is used to construct the Mt-Na^+ system considering a multilayer system with the convergence criterion for the electronic band structures in the Mt-Na^+ system considered in the limit of large supercells. After increasing the supercell size, we found that the 41-atom supercell is large enough to perform accurate calculations with periodic boundary conditions. Due to the use of a large supercell, the self-consistent calculations were performed at the gamma point only. On the other hand, for density-of-state calculations, a 4 × 2 × 2 Monkhorst−Pack[53] k-point mesh was adopted for the Brillouin zone (BZ) integrations. All of the calculations were performed with a 450 eV energy cutoff in the planewave expansions. The equilibrium structure for each case was obtained through ionic relaxations performed until the residual forces on the ions were less than 10 meV/Å.

DOI: 10.1021/acsomega.9b00685
ACS Omega 2019, 4, 14369−14377

3. RESULTS AND DISCUSSION

The calculations of the electronic structure of the $M_xAl_3Si_8O_{24}H_4Na$ clays were performed using a 41-atom supercell containing 4 H, 24 O, 3 Al, 8 Si, and 1 Na. The valence configuration of each atom is shown in Table 1. The montmorillonite has monoclinic structure and space group $C2/m$[14] with the expanded crystal structure of Mt-Na$^+$ shown in Figure 1.

Table 1. Electronic (Valence) Configuration of Each Atom Used in the Calculation

atom	valence electrons
H	$1s^1$
O	$2s^22p^4$
Al	$3s^23p^1$
Mg	$3s^2$
Si	$3s^23p^2$
Na	$3s^1$
Fe	$3d^64s^2$

According to Figure 1, Mt-Na$^+$ was simulated considering eight possible isomorphic substitutions with different configurations, namely, (C1) Mg_{Al1}, magnesium substituted for aluminum (Al1); (C2) Fe_{Al1}, iron substituted for aluminum (Al1); (C3) Fe_{Si1}, iron substituted for silicon (Si1); (C4) Fe_{Al1}−Fe_{Si1}, two irons substituted for aluminum (Al1) and silicon (Si1); (C5) Fe_{Al1}−Fe_{Si2}, two irons substituted for aluminum (Al1) and silicon (Si2); (C6) Fe_{Al1}−Fe_{Al2}, two irons substituted for two aluminum atoms (Al1 and Al2); (C7) Fe_{Al1}−Fe_{Al3}, two irons substituted for two aluminum atoms (Al1 and Al3); and (C8) Mg_{Al1}−Fe_{Al2}, one magnesium substituted for aluminum (Al1) and one iron substituted for aluminum (Al2).

After full relaxations, and in all cases, it was found that the stable configuration of the Na$^+$ cation is close to the oxygen atoms present on the upper surface of silica. This effect is related to the electrostatic attraction between lamellar and interlamellar cations. Around each Mg/Fe impurity site, there is an excess of negative charge −1 that needs to be compensated by sodium cation (charge +1) that are located in the interlamellar domain to establish the system's electroneutrality.[54] Lattice parameters (bond distances in Å and angles in degrees) were optimized for equivalent structures of dehydrated Mg-Mt-Na$^+$ (C1 case), producing a unit cell compatible with the experimental one. A good agreement between calculated and experimental results is observed. The basal spacing, c, equal to 10.08 Å is comparable with the theoretical range 10.06−10.28 Å[32,33] and with experimental interval 9.83−12.1 Å.[55,56] It was observed that the Al−O bond lengths are longer than the Si−O bond lengths, indicating that Al−O bonds are weaker in strength than the Si−O bonds, thus indicating that it is more probable to find montmorillonites composed of mixed octahedrons. A complete comparison between structural constants of dehydrated montmorillonite Mg-Mt-Na$^+$ and experimental results is shown in Table 2.

Table 2. Minimized Lattice Parameters and Bond Lengths (in Å) for the 41-atom Mt-Na$^+$ Supercells[a]

	this work	other theoretical works[32,36]	experimental[55,56]
a	5.41	5.208	5.18
b	9.00	9.020	8.97−9.01
c	10.08	10.28	9.83−12.1
Si−O/Å	1.65	1.634	1.63
Al−O/Å	1.94	1.913	1.75
H−O/Å	0.96	0.978	0.958
O−Si−O/°	108.6	109.5	109.5

[a]Experimental results from the literature are also shown.

Figure 2a shows the band structure of Mg-Mt-Na$^+$ along the high-symmetry lines in the BZ obtained from GGA-PBE functional.[46] A zoomed plot around the band gap region is shown in Figure 2b. The calculation was done in the first BZ on the path Y−A−Γ−Y−M−Γ−V−L− Γ, as depicted in Figure 2c. The band structure presented in Figure 2b indicates that the conduction-band minimum (CBM) (lowest unoccupied molecular orbital) is at the V-point and the valence-band maximum (VBM) (highest occupied molecular orbital) is at the Γ-point. Thus, the montmorillonite isomorphically substituted with Mg depicts a band gap of 4.63 eV, which implies that it is a material with insulating characteristics. This result is in good agreement with other theoretical results found in the literature.[36,57,58]

The projected density of states (PDOS) for Mg, Al, O, H, Si, and Na are shown in Figure 3, together with the total density

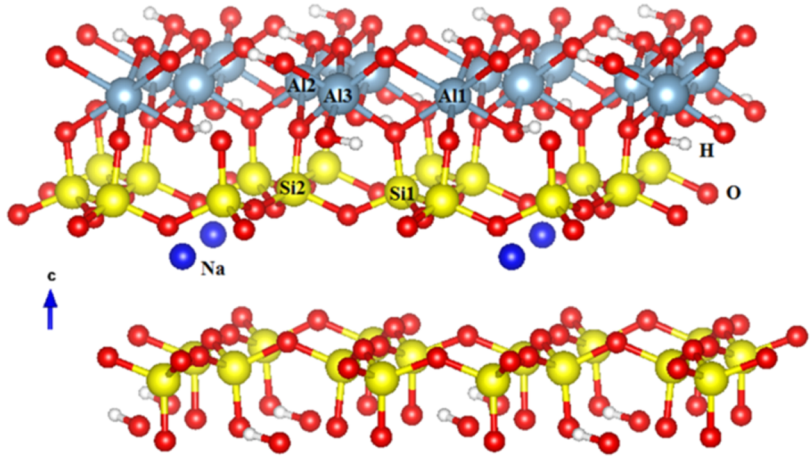

Figure 1. Expanded cell structure of the sodium montmorillonite Mt-Na$^+$. Al1, Al2, Al3, Si1, and Si2 are sites where the iron impurity was introduced.

DOI: 10.1021/acsomega.9b00685
ACS Omega 2019, 4, 14369−14377

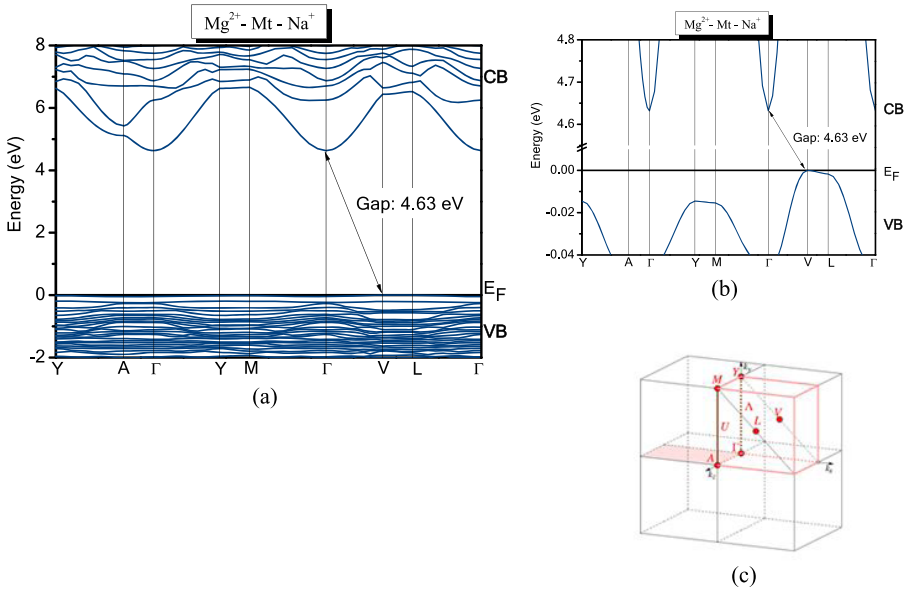

Figure 2. (a) GGA-PBE calculated band structure of montmorillonite with magnesium substituted for aluminum. VB stands for the valence band and CB stands for the conduction band. The Fermi (E_F) level is at the zero energy; (b) zoomed around the band gap region and (c) description of the *k*-points *Y* (0.5; 0.5; 0), *A* (0; 0; 0.5), Γ (0; 0.5), *V* (0.5; 0; 0), and *L* (0.5; 0; 0.5) in the first Brillouin zone.

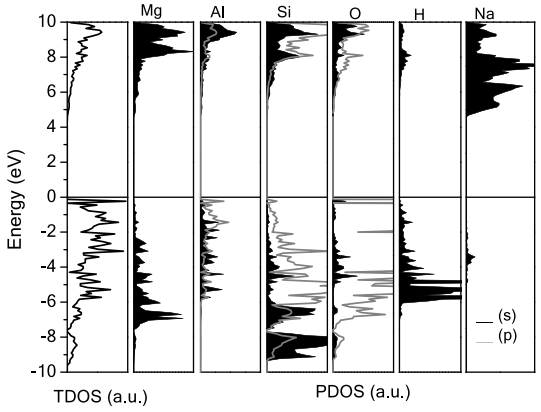

Figure 3. GGA-PBE calculated projected density of states (PDOS) and total density of states (TDOS) for the Mg-Mt-Na$^+$ compound. The Fermi (E_F) level is at the zero energy.

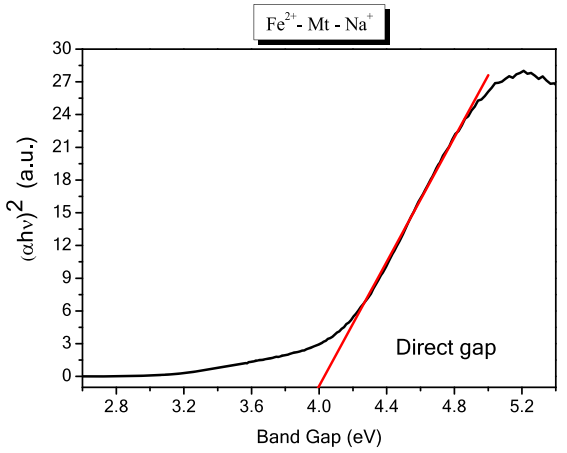

Figure 4. Band gap energy of Fe-doped Mt-Na$^+$ determined from the Tauc method.

of states (TDOS) for Mg^{2+}-Mt-Na^+. The upper part of the VB has mainly O-p orbital character, while the CB bottom has a higher character of Na-s orbitals. These results for $MgAl_3Si_8O_{24}H_4Na$ are in good accordance with experimental data as well as previous theoretical results available in the literature.[26,36,57]

Figure 4 shows the results of UV−vis spectroscopy measurements performed with pristine sodium Mt clays (Cloisite-Na$^+$), which has in its composition Si, Al, Fe, O, H, and Na. To determine the size of the band gap energy, we carried out spectroscopy measurements in the UV−vis region using the powdered clay sample. The band gap energy (E_g) was estimated by the Tauc method from absorbance data.[37−39] A direct band gap energy E_g = 4.0 eV was determined by extrapolating the linear region $(\alpha h\upsilon)^2$ versus photon energy.

In contrast, Figure 5 shows for Fe-Mt-Na$^+$ (C2 case) the calculated band structure of montmorillonite along the high-symmetry lines of the BZ using the GGA-PBE for the exchange−correlation potential. The obtained band gap energy (∼1.4 eV) is much smaller than the experimental value, thus

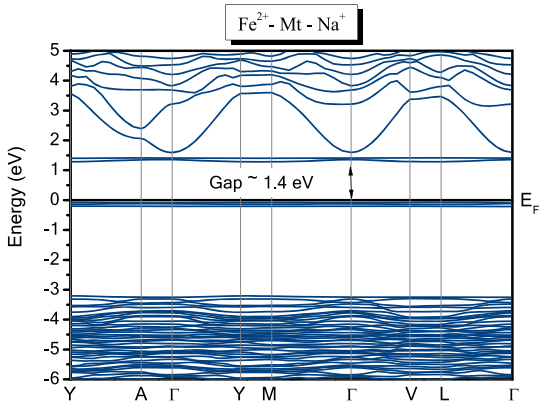

Figure 5. Band structure, along high-symmetry lines of the BZ, for Fe-doped montmorillonite as obtained by GGA-PBE calculations for case C2. The Fermi level (E_F) is at the zero energy.

DOI: 10.1021/acsomega.9b00685
ACS Omega 2019, 4, 14369−14377

leading to the conclusion that the GGA-PBE approach alone is not sufficient to determine the band gap energy of Fe-Mt-Na$^+$.

To obtain a better result of the band gap energy, calculations were performed using the mBJ approach wherein the value for the band gap found to be 7.0 eV, which is too large when compared to the experimental result found by the Tauc method. Another improvement made toward improving the description of the Fe-Mt-Na$^+$ band gap was to perform calculations including the exact components of the exchange energy as obtained via the Hartree−Fock method by means of the hybrid functional (HSE06). A suitable result of 4.3 eV was obtained as compared with the experimental value presented in Figure 4.

As shown in Figure 6, both the conduction-band minimum (CBM) and the valence-band maximum (VBM) are at the Γ

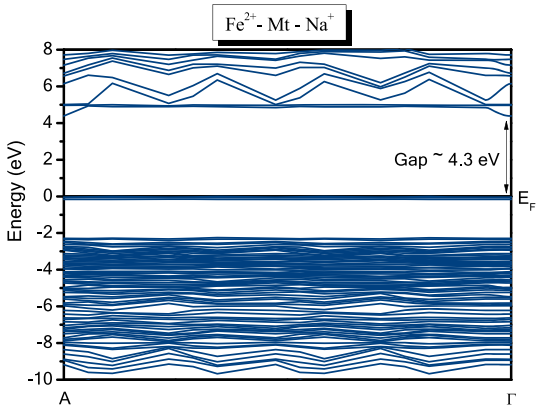

Figure 6. Band structure of iron-doped montmorillonite along the high-symmetry direction $A \rightarrow \Gamma$, as obtained through the hybrid functional (HSE06) calculations for case C2.

point, indicating a direct gap of 4.3 eV. Therefore, HSE06 is the most appropriate approach to correctly describe the electronic structure of the Fe-Mt-Na$^+$ system in the C2 configuration. As the hybrid functional calculations require a larger computational cost, the band structures shown in Figure 6 were performed only for the $A \rightarrow \Gamma$ path. The flat bands have iron d-level character.

Figure 7 shows the TDOS and PDOS obtained for the Fe-Mt-Na$^+$ system using GGA-PBE. We observe that the valence bands in a wide energy range -12.5 eV $< E < E_F$ are

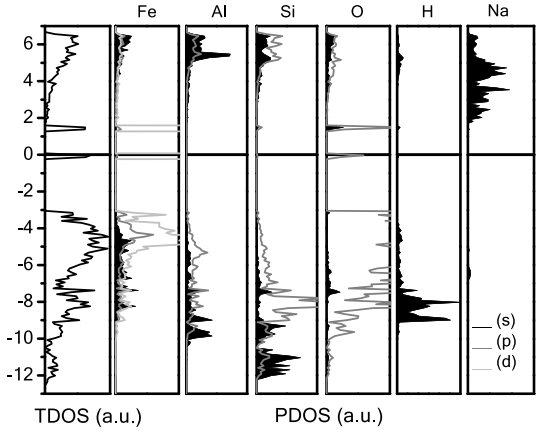

Figure 7. TDOS and PDOS of montmorillonite obtained with GGA-PBE for case C2. The Fermi energy is set to zero.

predominantly composed of oxygen p-orbitals. Since iron introduces energy levels in the upper part of the VB, it causes repulsion with the electrons arising from oxygen atoms pushing up the iron-related levels to higher energies. This gives rise to an internal gap of about 3.0 eV (2.0 eV) obtained from the GGA-PBE (HSE06) calculations.

Figure 8 shows the charge density plot of the atoms occupying sites that influence the band gap region. Both the

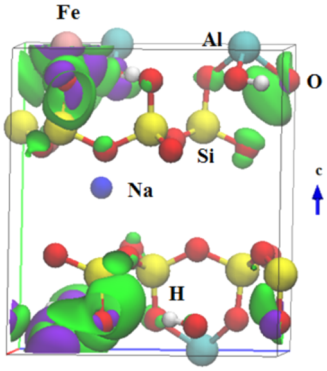

Figure 8. Charge density plot associated with the uppermost occupied valence band state (purple) and probability density of the first unoccupied conduction band state (green), for case C2. Both states have mainly oxygen p and iron d orbital character.

charge density of the uppermost occupied VB state and the probability density of the first unoccupied CB state have mainly oxygen p and iron d orbital character. When iron is added to the compound, it becomes mostly responsible for the majority of the charge density distribution shown, placing occupied and unoccupied d-related levels close to the top of the valence and the CB bottom, respectively.

To estimate the oxidation state of Fe-substituting Al1 for case C2, an analysis of the local coordination and the number of unpaired electrons was done via magnetic moment calculation. The d orbitals of the iron impurity are split by the crystalline field in the material, and due to the octahedral field (Fe_{Al1}), gives rise to a tridegenerate t_{2g} and a bidegenerate e_g level. The difference in energy between the t_{2g} and e_g levels is about 1.4 eV using GGA-PBE. Figure 9 shows the PDOS related to the Fe d-derived energy levels of t_{2g} and e_g symmetries of montmorillonite, as obtained in the GGA-PBE calculations. A magnetic moment of ∼4 μ_B was found, demonstrating a 2+ (Fe^{2+}) oxidation state. Fe^{2+} substituting an Al^{3+} is in agreement with electroneutrality requirement,

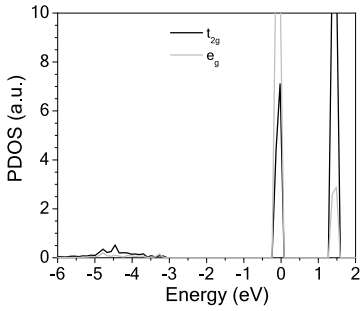

Figure 9. PDOS associated with the Fe d-derived energy levels of t_{2g} and e_g symmetries of montmorillonite, obtained using GGA-PBE, for case C2. The Fermi energy is set to zero.

DOI: 10.1021/acsomega.9b00685
ACS Omega 2019, 4, 14369−14377

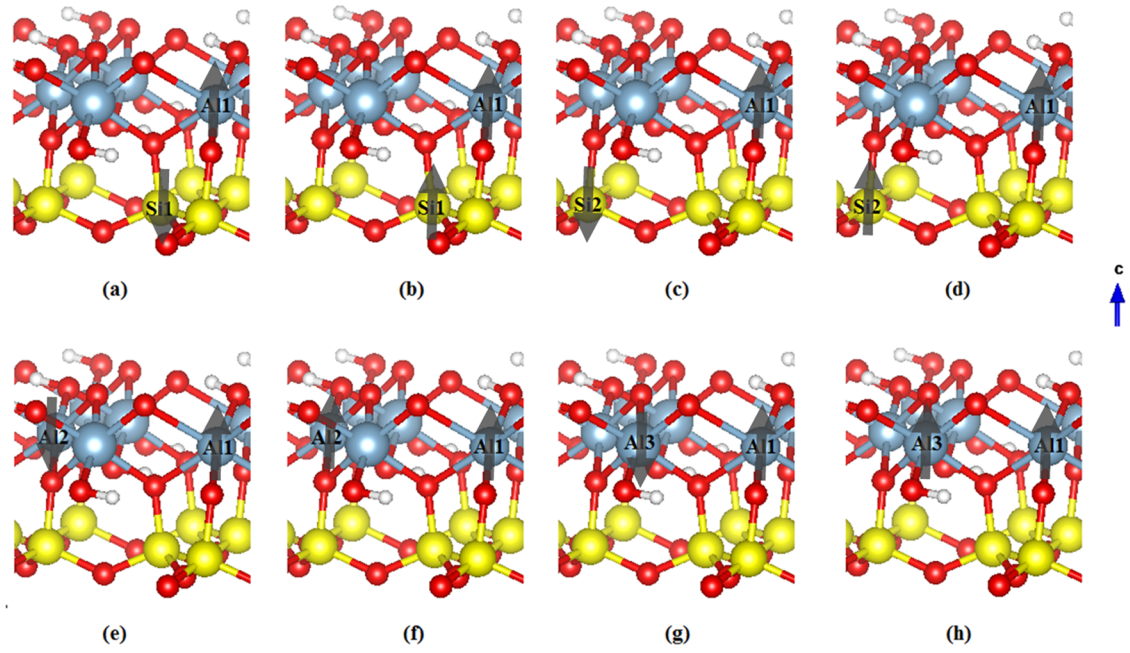

Figure 10. HSE06-calculated magnetic state possibilities for configurations C4 (a) AFM and (b) FM; C5 (c) AFM and (d) FM; C6 (e) AFM and (f) FM; and C7 (g) AFM and (h) FM.

which means a negative charge excess (−1e) from each Fe^{2+} substitution to neutralize the positive charge from the intercalated sodium cation (Na^+). This charge excess is delocalized almost uniformly all over the basal oxygen atoms of the silica surface, which attracts the sodium atoms. Therefore, this result clearly indicates that the location of Na^+ cation close to the clay surface is governed by the presence of negative charge centers in the clay materials.[32,54] The same value of magnetic moment (~4 μ_B) was obtained from the HSE06 calculations; however, as expected, disagreement occurred for the energy difference between t_{2g} and e_g levels that showed a more realistic value, ~5 eV, as revealed in Figure 6.

To seek a more complete understanding of oxidation states of the iron impurity taking in place at different sites in the Mt-Na^+ material, a similar oxidation state analysis was performed for cases ranging from C3 to C8 configurations. In case C3, for Fe substitution for Si^{4+} at a tetrahedral site, the magnetic moment of ~5 μ_B was obtained from GGA-PBE and HSE06 calculations, indicating a 3+ (Fe^{3+}) oxidation state, meaning that a negative charge excess from each Fe^{3+} substitution neutralizes the positive charge from the intercalated Na^+. The obtained energy difference between e_g and t_{2g} levels is about 4.7 eV.

An increase of iron impurity concentration was simulated from C4 to C7 configurations, highlighting for C4 (Fe_{Al1}−Fe_{Si1}), two irons substituted for aluminum (Al1) and silicon (Si1); C5 (Fe_{Al1}−Fe_{Si2}), two irons substituted for aluminum (Al1) and silicon (Si2); C6 (Fe_{Al1}−Fe_{Al2}), two irons substituted for two aluminums (Al1 and Al2); and C7 (Fe_{Al1}−Fe_{Al3}), two irons substituted for two aluminums (Al1 and Al3). For each case, two different distances between impurities as well as the ferromagnetic (FM) and antiferromagnetic (AFM) configurations were considered, as shown in Figure 10. The AFM configuration was the most stable for the C4 and C5 cases. For both cases, the magnetic moments of iron substituted for aluminum and silicon are 5.0μ_B, which means a 3+ oxidation state (Fe^{3+}) as expected. The C4 and C5 cases also show that a negative charge excess from Fe^{3+} substituted for Si^{4+} neutralizes the positive charge from the intercalated Na^+. No charge excess happens to other Fe^{3+} substituted for Al^{3+}.

For the C6 and C7 cases, an FM state was observed and the magnetic moment of the two Fe substituted for two Al was 4.0 μ_B with a 2+ oxidation state (Fe^{2+}) for the first and 1.0 μ_B with oxidation state 3+ (Fe^{3+}) for the second. For both configurations, a negative charge excess from Fe^{2+} substituted for the first aluminum Al^{3+} neutralizes the positive charge from the intercalated Na^+. No charge excess occurs for Fe^{3+} substituted for a second Al^{3+}.

For both pairs C4, C5 and C6, C7, the oxidation states did not depend on the distance between iron impurities, even having an oxygen atom shared as shown for cases C4 (Al1−O−Si1) and C7 (Al1−O−Al3). Table 3 shows a summary of oxidation states for all cases.

For C8 configuration, in which one magnesium replaces one aluminum (Al1) and one iron replaces one aluminum (Al2), after a full relaxation, a magnetic moment equal to 5 μ_B for the iron atom was obtained. This result shows that iron has an oxidation state equal to 3+ (Fe^{3+}) in substitution of aluminum 3+ (Al^{3+}). On the other hand, magnesium has an oxidation state equal to 2+ (Mg^{2+}), being responsible to neutralize the positive charge from the intercalated Na^+.

4. CONCLUSIONS

The structural and electronic properties of magnesium- and iron-doped montmorillonite in several configurations were studied through first-principles calculations using density functional theory. The results obtained for Mg^{2+}-Mt-Na^+ using GGA-PBE indicated an underestimation of the band gap energy at 4.63 eV. For a single iron substituted for aluminum (C2 configuration), the underestimated GGA-PBE band gap energy of only ~1.4 eV was obtained. Using the hybrid functional (HSE06) approach, a value of 4.3 eV was

DOI: 10.1021/acsomega.9b00685
ACS Omega 2019, 4, 14369−14377

Table 3. HSE06-Calculated Iron Oxidation States, Magnetic Moment (m_{Fe}), and Magnetic State of Mt-Na^+ in C2, C3, C4, C5, C6, C7, and C8 Configurations[a]

conf.	impurity	m_{Fe} (μ_B)	oxidation state	magnetic state
C2	Fe_{Al1}	4.0	Fe^{2+}	
C3	Fe_{Si1}	5.0	Fe^{3+}	
C4	Fe_{Al1}	5.0	Fe^{3+}	AFM
	Fe_{Si1}	−5.0	Fe^{3+}	
C5	Fe_{Al1}	5.0	Fe^{3+}	AFM
	Fe_{Si2}	−5.0	Fe^{3+}	
C6	Fe_{Al1}	4.0	Fe^{2+}	FM
	Fe_{Al2}	1.0	Fe^{3+}	
C7	Fe_{Al1}	4	Fe^{2+}	FM
	Fe_{Al3}	1	Fe^{3+}	
C8	Mg_{Al1}	0	Mg^{2+}	
	Fe_{Al3}	1	Fe^{3+}	

[a]FM and AFM stand for ferromagnetic and antiferromagnetic configurations, respectively.

found, in excellent agreement with the value obtained from ultraviolet−visible (UV−vis) spectroscopy measurements of 4.0 eV. The charge density and the density of states alongside the magnetic moment analysis have shown that the oxidation state of the iron impurity substituted for Al^{3+} is 2+ (Fe^{2+}) and introduces d-related energy levels in the band gap of the material, giving the material a semiconductor character. The electroneutrality of the system was established via magnetic moment and magnetic state analysis, and it was found that both Fe^{2+} and Fe^{3+} oxidation states are possible to occur, where the state depends only on the site iron occupies in the Mt-Na^+ structure. For cases C4 and C5, both iron impurities have oxidation state 3+. In the cases C6 and C7, a mixing of iron impurities with oxidation states 2+ and 3+ was observed. For case C8, where one magnesium substitutes one aluminum (Al1) and one iron substitutes one aluminum (Al2), iron has an oxidation state equal to 3+ (Fe^{3+}) in substitution of aluminum 3+ (Al^{3+}) and magnesium has an oxidation state equal to 2+ that is responsible to neutralize the positive charge from the intercalated Na^+.

5. EXPERIMENTAL SECTION

UV−Vis Spectroscopy. Optical absorption spectroscopy measurements are fundamental tools in the study of electronic properties of materials, mainly semiconductors. In this context, ultraviolet−visible spectroscopy (UV−vis) offers a convenient method to estimate the optical band gap since it probes electronic transitions between the valence band and the conduction band by diffuse reflectance spectra. Diffuse reflection comprises a process that occurs when radiation penetrates a solid substrate. Part of this radiation returns to the surface of the substrate, also causing multiple dispersion and partial absorption of the radiation by the particles or fibers that constitute the solid substrate. In this case, the band gap is determined from Tauc plots obtained from diffuse reflectance spectra.[37] The absorption coefficient (α) was determined from optical absorption data and the nature of the transition by plotting graphs of $(\alpha h\upsilon)^2$ as a function of the energy of the incident photon ($h\upsilon$), with υ being the frequency and h being the Plank constant. The band gap energy is determined by the intersection point of the tangent line to the point of inflection of the curve and the horizontal axis.[38,39]

A sample of natural montmorillonite containing Si, Al, Fe, O, H, and Na from Southern Clay Products Inc., Texas, was used for the absorption spectroscopy measurements in the UV−vis region aiming to determine the experimental optical band gap value. Absorption spectra analysis of the powdered clay was performed using a Lambda 1050 UV/vis spectrophotometer (PerkinElmer), programmed for the reflectance mode with wavelengths in the range of 200−800 nm. Since experimental setup must be constructed with a reference that fully reflects light such that the largest wavelength possible has a reflectance equal to 1, magnesium oxide (MgO) was adopted as a reference material due to its absolute reflectance in the visible range (0.98).[40]

■ ASSOCIATED CONTENT

Supporting Information

The Supporting Information is available free of charge on the ACS Publications website at DOI: 10.1021/acsomega.9b00685.

X-ray photoelectron spectroscopy and chemical composition data (Table S1, Table S2), as well as Fourier transform infrared spectra and X-ray diffraction pattern of montmorillonite clay (Figure S1, Figure S2) (PDF)

■ AUTHOR INFORMATION

Corresponding Author

*E-mail: pdborges@gmail.com. Tel: (+55) 34 991 87 98 70.

ORCID

Camila R. Ferreira: 0000-0002-3254-6599

Pablo D. Borges: 0000-0003-3829-5134

Notes

The authors declare no competing financial interest.

■ ACKNOWLEDGMENTS

Authors thank CAPES, CNPq and FAPESP Brazilian funding agencies for the financial support of this work. We also acknowledge Texas State University for providing infrastructure for the calculations through the high-performance computational center (LEAP). We would like to further thank Samuel Cantrell from the Department of Physics, at Texas State University, for carefully reviewing the English.

■ REFERENCES

(1) Jha, A.; Garade, C.; Shirai, M.; Rode, C. Metal cation-exchanged montmorillonite clay as catalysts for hydroxyalkylation reaction. *Appl. Clay Sci.* **2013**, *74*, 141−146.

(2) Zhang, D.; Zhou, C. H.; Lin, C. X.; Tong, D. S.; Yu, W. H. Synthesis of clay minerals. *Appl. Clay Sci.* **2010**, *50*, 1−11.

(3) Bergaya, F.; Lagaly, G. General introduction: Clays, clay minerals, and clay science. In *Handbook of Clay Science*, Bergaya, F., Theng, B. K. G., Lagaly, G., Eds.; Elsevier Science and Technology: Oxford, 2006; pp 1−18.

(4) Uddin, F. Montmorillonite: An introduction to properties and utilization. In *Current Topics in the Utilization of Clay in Industrial and Medical Applications*, Zoveidavianpoor, M., Ed.; IntechOpen: London, 2018; pp 4−23.

(5) Sainz-Díaz, C. I.; Palin, E. J.; Hernández-Laguna, A.; Dove, M. T. Octahedral cation ordering of illite and smectite. Theoretical exchange potential determination and Monte Carlo simulations. *Phys. Chem. Miner.* **2003**, *30*, 382−392.

(6) Hernández-Laguna, A.; Escamilla-Roa, E.; Timón, V.; Dove, M. T.; Sainz-Díaz, C. I. DFT study of the cation arrangements in the

DOI: 10.1021/acsomega.9b00685
ACS Omega 2019, 4, 14369−14377

octahedral and tetrahedral sheets of dioctahedral 2:1 phyllosilicates. *Phys. Chem. Miner.* **2006**, *33*, 655−666.
(7) Sainz-Díaz, C. I.; Palin, E. J.; Dove, M. T.; Hernández-Laguna, A. Monte Carlo simulations of ordering of Al, Fe, and Mg cations in the octahedral sheet of smectites and illites. *Am. Mineral* **2003**, *88*, 1033−1045.
(8) Mignon, P.; Ugliengo, P.; Sodupe, M.; Hernandez, E. R. Ab initio molecular dynamics study of the hydration of Li^+, Na^+ and K^+ in a montmorillonite model. Influence of isomorphic substitution. *Phys. Chem. Chem. Phys.* **2010**, *12*, 688−697.
(9) Carvalho, H. W.; Santilli, C. V.; Briois, V.; Pulcinelli, S. H. Polymer−clay nanocomposites thermal stability: Experimental evidence of the radical trapping effect. *RSC Adv.* **2013**, *3*, 22830−22833.
(10) Carvalho, H. W. P. D.; Leroux, F.; Briois, V.; Santilli, C. V.; Pulcinelli, S. H. Thermal stability of PMMA−LDH nanocomposites: Decoupling the physical barrier, radical trapping, and charring contributions using XAS/WAXS/Raman time-resolved experiments. *RSC Adv.* **2018**, *8*, 34670−34681.
(11) Polubesova, T.; Chen, Y.; Navon, R.; Chefetz, B. Interactions of hydrophobic fractions of dissolved organic matter with Fe^{3+}-and Cu^{2+}-montmorillonite. *Environ. Sci. Technol.* **2008**, *42*, 4797−4803.
(12) Chang, J.; Ma, J.; Ma, Q.; Zhang, D.; Qiao, N.; Hu, M.; Ma, H. Adsorption of methylene blue onto Fe_3O_4/activated montmorillonite nanocomposite. *Appl. Clay Sci.* **2016**, *119*, 132−140.
(13) Cottet, L.; Almeida, C. A. P.; Naidek, N.; Viante, M. F.; Lopes, M. C.; Debacher, N. A. Adsorption characteristics of montmorillonite clay modified with iron oxide with respect to methylene blue in aqueous media. *Appl. Clay Sci.* **2014**, *95*, 25−31.
(14) Newman, A. C. D.; Brown, G. The chemical constitution of clays. In *Chemistry of Clays and Clay Minerals*, Longman Scientific and Technical: London, 1987; pp 1−28.
(15) Ray, C.; Ramsey, R. H. Removal of heavy metals in wastewater in a clay soil matrix using electro-osmosis. *Environ. Prog.* **1987**, *6*, 145−149.
(16) Pinnavaia, T. J. Intercalated clay catalysts. *Science* **1983**, *220*, 365−371.
(17) Mansoori, Y.; Atghia, S. V.; Sanaei, S. S.; Zamanloo, M. R.; Imanzadeh, G. PMMA-clay nanocomposite materials: Free-radically grafting of PMMA onto organophilic montmorillonite (20A). *Macromol. Res.* **2010**, *18*, 1174−1181.
(18) Carvalho, H. W.; Suzana, A. F.; Santilli, C. V.; Pulcinelli, S. H. Synthesis, structure, and thermal stability of poly(methyl methacrylate)-co-poly (3-tri(methoxysilyil) propyl methacrylate)/montmorillonite nanocomposites. *Polym. Eng. Sci.* **2013**, *53*, 1253−1261.
(19) Gorb, L.; Gu, J.; Leszczynska, D.; Leszczynski, J. The interaction of nitrobenzene with the hydrate basal surface of montmorillonite: An ab initio study. *Phys. Chem. Chem. Phys.* **2000**, *2*, 5007−5012.
(20) Fan, Y. Q. Cation diffusion and conduction in solid electrolytes Li, Na-montmorillonites. *Solid State Ionics* **1988**, *28*−*30*, 1596−1601.
(21) Tavares, S. R.; Vaiss, V. S.; Antunes, F. P. N.; Fonseca, C. G.; Nangoi, I. M.; Moraes, P. I. R.; Soares, C. V.; et al. DFT calculations for structural prediction and applications of intercalated lamellar compounds. *Dalton Trans.* **2018**, *47*, 2852−2866.
(22) Costa, D. G.; Rocha, A. B.; Souza, W. F.; Chiaro, S. S. X.; Leitão, A. A. Ab initio simulation of changes in geometry, electronic structure, and Gibbs free energy caused by dehydration of hydrotalcites containing Cl^- and CO_3^{2-} counter anions. *J. Phys. Chem. B* **2011**, *115*, 3531−3537.
(23) Peng, C.; Min, F.; Liu, L.; Chen, J. A periodic DFT study of adsorption of water on sodium-montmorillonite (001) basal and (010) edge surface. *Appl. Surf. Sci.* **2016**, *387*, 308−316.
(24) Zheng, Y.; Zaoui, A. Mechanical behavior in hydrated Na-montmorillonite clay. *Phys. A (Amsterdam, Neth.)* **2018**, *505*, 582−590.
(25) Fonseca, C. G.; Vaiss, V. S.; Wypych, F.; Diniz, R.; Leitão, A. A. Structural and thermodynamic investigation of the hydration-dehydration process of Na^+-Montmorillonite using DFT calculations. *Appl. Clay Sci.* **2017**, *143*, 212−219.
(26) Pirillo, S.; Luna, C. R.; López-Corral, I.; Juan, A.; Avena, M. J. Geometrical and electronic properties of hydrated sodium montmorillonite and tetracycline montmorillonite from DFT calculations. *J. Phys. Chem. C* **2015**, *119*, 16082−16088.
(27) Peng, C.; Min, F.; Liu, L.; Chen, J. The adsorption of $CaOH^+$ on (001) basal and (010) edge surface of Na-montmorillonite: A DFT study. *Surf. Interface Anal.* **2017**, *49*, 267−277.
(28) Escamilla-Roa, E.; Huertas, F. J.; Hernández-Laguna, A.; Sainz-Díaz, C. I. A DFT study of the adsorption of glycine in the interlayer space of montmorillonite. *Phys. Chem. Chem. Phys.* **2017**, *19*, 14961−14971.
(29) Peng, C.; Zhong, Y.; Min, F. Adsorption of alkylamine cations on montmorillonite (001) surface: A density functional theory study. *Appl. Clay Sci.* **2018**, *152*, 249−258.
(30) Liao, L.; Lv, G.; Cai, D.; Wu, L. The sequential intercalation of three types of surfactants into sodium montmorillonite. *Appl. Clay Sci.* **2016**, *119*, 82−86.
(31) Rebaza, A. V. G.; Montes, M. L.; Taylor, M. A.; Errico, L. A.; Alonso, R. E. Experimental and theoretical study of Co sorption in clay montmorillonites. *Mater. Res. Express* **2018**, *5*, No. 035519.
(32) Fonseca, C. G.; de Carvalho, G. S.; Wypych, F.; Diniz, R.; Leitão, A. A. Na^+ as a probe to structural investigation of dehydrated smectites using NMR spectra calculated by DFT. *Appl. Clay Sci.* **2016**, *126*, 132−140.
(33) Liu, P. Polymer modified clay minerals: A review. *Appl. Clay Sci.* **2007**, *38*, 64−76.
(34) Borges, P. D.; Silva, D. E. S.; Castro, N. S.; Ferreira, C. R.; Pinto, F. G.; Tronto, J.; Scolfaro, L. Ab initio study of thermoelectric properties of doped SnO_2 superlattices. *J. Solid State Chem.* **2015**, *231*, 123−131.
(35) Shi, J.; Liu, H.; Lou, Z.; Zhang, Y.; Meng, Y.; Zeng, Q.; Yang, M. Effect of interlayer counter ions on the structures of dry montmorillonites with Si^{4+}/Al^{3+} substitution. *Comput. Mater. Sci.* **2013**, *69*, 95−99.
(36) Man-Chao, H.; Zhi-Jie, F.; Ping, Z. Atomic and electronic structures of montmorillonite in soft rock. *Chin. Phys. B* **2009**, *18*, 2933−2937.
(37) Makuła, P.; Pacia, M.; Macyk, W. How to correctly determine the band gap energy of modified semiconductor photocatalysts based on UV−vis spectra. *J. Phys. Chem. Lett.* **2018**, *9*, 6814−6817.
(38) Tauc, J. *Optical Properties of Solids*, Abeles: North-Holland, Amsterdam, 1972; pp 159−220.
(39) Tauc, J.; Grigorovic, R.; Vancu, A. Optical properties and electronic structure of amorphous germanium. *Phys. Status Solidi B* **1966**, *15*, 627−637.
(40) Workman, J., Jr. Ultraviolet, visible, and near-infrared spectrometry. In *Applied Spectroscopy: A Compact Reference for Practitioners*, Workman, J., Jr.; Springsteen, W. A., Eds.; Academic Press: New York, 1998; pp 28−29.
(41) Jensen, F. An introduction to the state of the art in quantum chemistry. *Annu. Rep. Comput. Chem.* **2005**, *1*, 3−17.
(42) Szabo, A.; Ostlund, N. S. Many electron ware functions and operators. In *Modern Quantum Chemistry: Introduction to Advanced Electronic Structure Theory*, Dover Publications: New York, 1996; pp 40−53.
(43) Hohenberg, P.; Kohn, W. Inhomogeneous electron gas. *Phys. Rev.* **1964**, *136*, B864−B871.
(44) Kohn, W.; Sham, L. J. Self-consistent equations including exchange and correlation effects. *Phys. Rev.* **1965**, *140*, A1133−A1138.
(45) Blöchl, P. Projector augmented-wave method. *Phys. Rev. B* **1994**, *50*, 17953−17979.
(46) Perdew, J. P.; Burke, K.; Ernzerhof, M. Generalized gradient approximation made simple. *Phys. Rev. Lett.* **1996**, *77*, No. 3865.
(47) Tran, F.; Blaha, P. Accurate band gaps of semiconductors and insulators with a semilocal exchange-correlation potential. *Phys. Rev. Lett.* **2009**, *102*, No. 226401.

DOI: 10.1021/acsomega.9b00685
ACS Omega 2019, 4, 14369−14377

(48) Becke, A. D. Density-functional thermochemistry. III. The role of exact exchange. *J. Chem. Phys.* **1993**, *98*, No. 5648.
(49) Heyd, J.; Scuseria, G. E.; Ernzerhof, M. Hybrid functionals based on a screened Coulomb potential. *J. Chem. Phys.* **2003**, *118*, 8207−8215.
(50) Kresse, G.; Marsman, M.; Furthmuller, J.*Vienna Ab-initio Simulation Package (VASP): VASP the Guide Computacional Physics*, University of Vienna: Vienna, 2012; pp 1−188.
(51) Kresse, G.; Furthmuller, J. Efficiency of ab-initio total energy calculations for metals and semiconductors using a plane-wave basis set. *Comput. Mater. Sci.* **1996**, *6*, 15−50.
(52) Kresse, G.; Furthmuller, J. Efficient iterative schemes for ab initio total-energy calculations using a plane-wave basis set. *Phys. Rev. B.* **1996**, *54*, 11169−11186.
(53) Monkhorst, H.; Pack, J. D. Special points for Brillouin-zone integrations. *Phys. Rev. B* **1976**, *13*, 5188−5192.
(54) Chatterjee, A.; Iwasaki, T.; Ebina, T.; Miyamoto, A. A DFT study on clay−cation−water interaction in montmorillonite and beidellite. *Comput. Mater. Sci.* **1999**, *14*, 119−124.
(55) Sato, T.; Watanabe, T.; Otsuka, R. Effects of layer charge, charge location and energy change on expansion properties of dioctahedral smectites. *Clays Clay Miner.* **1992**, *40*, 103−113.
(56) Tsipursky, S.; Drits, V. The distribution of octahedral cations in the 2:1 layers of dioctahedral smectites studied by oblique-texture electron diffraction. *Clay Miner.* **1984**, *19*, 177−193.
(57) Wungu, T. D. K.; Aspera, S. M.; David, M. Y.; Dipojono, H. K.; Nakanishi, H.; Kasai, H. Absorption of lithium in montmorillonite: A density functional theory (DFT) study. *J. Nanosci. Nanotechnol.* **2011**, *11*, 2793−2801.
(58) Wang, Q.; Zhu, C.; Yun, J.; Yang, G. Isomorphic substitutions in clay materials and adsorption of metal ions onto external surfaces: A DFT investigation. *J. Phys. Chem. C* **2017**, *121*, 26722−26732.

DOI: 10.1021/acsomega.9b00685
ACS Omega 2019, 4, 14369−14377